MAGIC: A label-free fluorescence method for 3D high-resolution reconstruction of myelinated fibers in large volumes

Irene Costantini[1,2*], Enrico Baria[1,3], Michele Sorelli[1,4], Felix Matuschke[5], Francesco Giardini[1,3], Miriam Menzel[5], Giacomo Mazzamuto[2,1], Ludovico Silvestri[1,3], Riccardo Cicchi[2,1], Katrin Amunts[5,6], Markus Axer[5], Francesco Saverio Pavone[1,2,3]

[1]European Laboratory for Non-linear Spectroscopy, University of Florence, Italy,

[2]National Institute of Optics, National Research Council, Italy,

[3]Department of Physics, University of Florence, Italy,

[4]Department of Information Engineering, University of Florence, Italy,

[5]Institute of Neuroscience and Medicine (INM-1), Research Centre Jülich, Jülich, Germany,

[6]C. and O. Vogt Institute for Brain Research, University Hospital Düsseldorf, Heinrich-Heine University Düsseldorf, Germany

*corresponding author

Abstract

Analyzing the structure of neuronal fibers with single axon resolution, in large volumes, remains an unresolved challenge in connectomics. Here, we propose MAGIC (Myelin Autofluorescence imaging by Glycerol Induced Contrast enhancement), a simple tissue preparation method to perform label-free fluorescence imaging of myelinated fibers. We demonstrate its broad applicability by performing mesoscopic reconstruction at sub-micron resolution of mouse, rat, monkey, and human brain samples and by quantifying the different fiber organization in Control and Reeler mouse's hippocampal sections.

Main

The brain is a complex organ constituted by highly interconnected units, the neurons, capable of storing and processing information from a myriad of different inputs regulating most human activities. The aim of connectomics consists in reconstructing the intricate organization of the connections between brain regions at macro- to mesoscales, but also between individual neurons at the microscale. Most long-range projecting axons are wrapped by a myelin sheath to permit a reliable and efficient signal transmission[1]. Several methods have been developed to map the network of interneuronal connections; still, they are limited by the volume that they can analyze (Electron Microscopy)[2], by the spatial resolution achievable (MRI)[3] or by the

29 sophisticated equipment needed for the measurement (CARS, THG microscopy)[4]. Optical methods have the

30 potential for scalable large-area high-resolution mapping. However, they need a source of contrast to detect

31 the structure of interest. In this respect, myelin staining is an unmet technical challenge. Exogenous dyes[5]

32 are used to stain fibers composing the white matter, but nonspecific binding and inefficient diffusion of dyes

33 hinder single fiber imaging in large volumes.

34 To meet this need, we develop MAGIC (Myelin Autofluorescence imaging by Glycerol Induced Contrast

35 enhancement), a simple label-free method that opens the possibility of performing sub-micron resolution

36 fluorescence imaging of myelinated fibers in 3D at the mesoscale level. MAGIC is a methodology that enables,

37 with a glycerol-based procedure, to enhance myelin's autofluorescence, allowing the use of conventional

38 fluorescence microscopy techniques to investigate neuronal filament organization. Glycerol has been widely

39 used as a mounting and refractive index matching medium because of its biocompatibility[6]. We implemented

40 the MAGIC protocol from the observation that the removal of glycerol from previously fixed and embedded

41 tissue allows for the specific enhancement of myelin autofluorescence. MAGIC includes three steps (Figure

42 1a): fixation with paraformaldehyde (PFA), embedding in glycerol (Gly), and removal of glycerol by washing

43 in saline solution (MAGIC). During the procedure, myelinated fibers undergo a specific increase of

44 fluorescence efficiency, allowing for high-resolution 3D reconstruction of the axons (Figure 1b,

45 Supplementary Video 1). The number of emitted photons rises significantly during the different steps of the

46 protocol (Figure 1c). In PFA, we observed a negative contrast between fibers and surrounding tissue

47 fluorescence; instead, after the MAGIC protocol, the contrast becomes positive and is significantly increased

48 due to the raising of myelinated fiber autofluorescence (Figure 1d). The protocol does not introduce any

49 exogenous fluorophores and is based on the local enhancement of autofluorescence from endogenous

50 molecules. The fluorescence emitted from the myelinated fibers can be detected not only with two-photon

51 excitation but also with conventional one-photon microscopy. Supplementary figures display images

52 acquired with a commercial confocal microscope at various wavelengths (Supplementary Figure 1) and from

53 various species (Supplementary Figure 2). We demonstrate that the MAGIC protocol can provide details of

54   myelin substructures (Supplementary Figure 3) using a high-magnification objective and that it is also

55   compatible with conventional immunofluorescence (Supplementary Figure 4, Supplementary Video 2 and 3).

56   The spectral analysis of fluorescence signals reveals that the emission spectrum is not altered throughout the

57   steps of the protocol (Figure 1e). Nevertheless, the fluorescence signal from myelinated fibers is specifically

58   enhanced by MAGIC, as proved by the correlation with a mouse brain section labeled with an exogenous dye

59   specific for myelin staining: FluoroMyelin™ red[7]. The signal emitted by the dye perfectly overlaps the fibers'

60   autofluorescence signal, indicating that the fluorescence is indeed coming from myelin (Figure 1f).
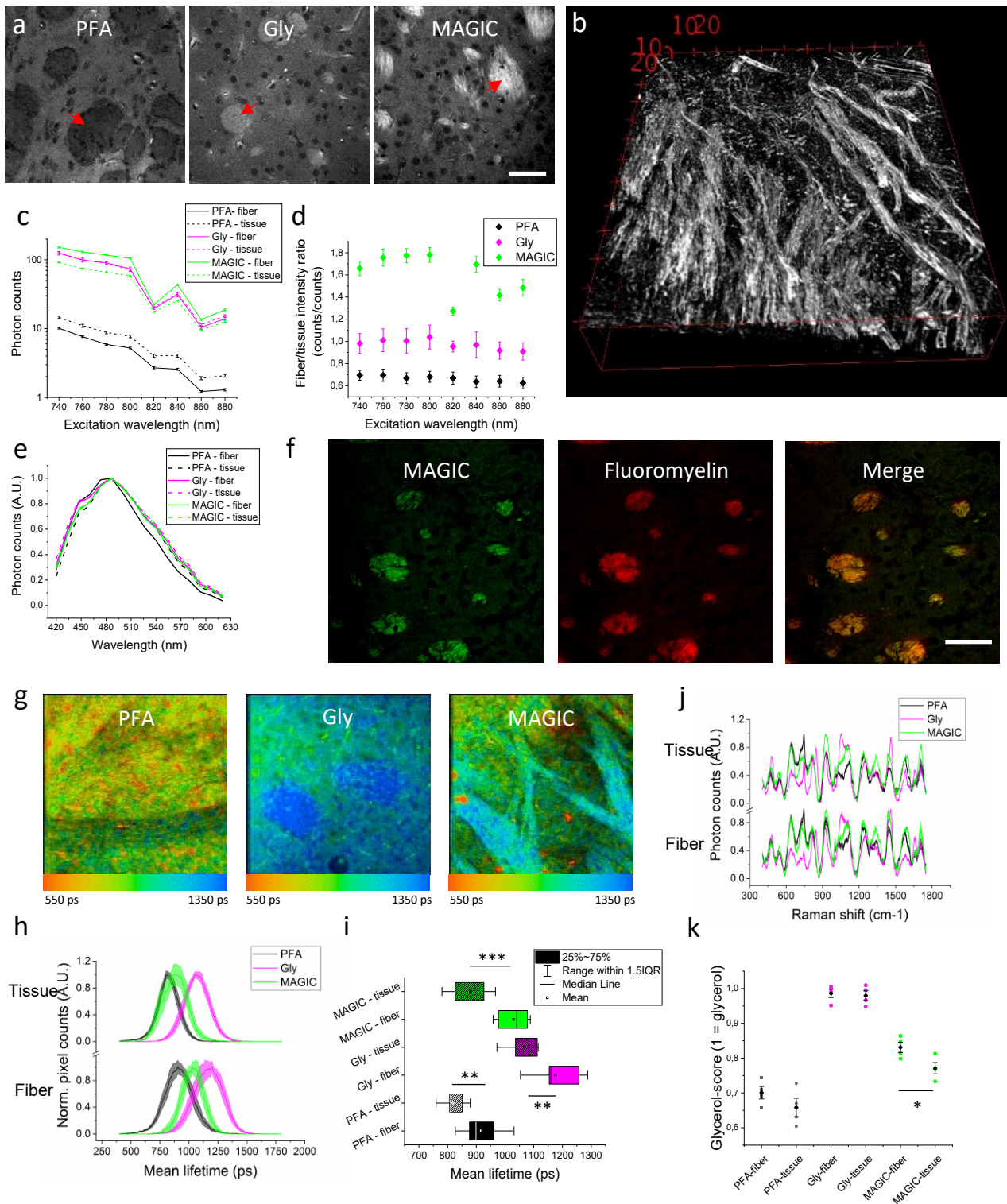
Figure 1. MAGIC: a method to perform label-free fluorescence imaging of myelinated fibers (a) Representative TPFM images of the caudate putamen of a mouse brain section during the three subsequent steps of the MAGIC protocol: fixation (PFA), glycerolization (Gly), and washing (MAGIC). Red arrows indicate fiber bundles. Scale bar = 50 µm. (b) 3D reconstruction of myelinated fibers, imaging performed with TPFM at the resolution of (0.44 x 0.44 x 1) µm^3. Box scale = 10 µm. (c) Measurement (mean ± std.err) of photons emitted by the myelinated fibers (fiber) and the surrounding tissue (tissue) during the different steps of the protocol (PFA, Gly, MAGIC) detected at different excitation wavelengths. (d) Intensity contrast (mean ± std.err) observed at different excitation wavelengths during the three steps of the MAGIC protocol. (e) Fluorescence emission spectra of the different samples excited with TPFM at 800 nm. (f) Images of a mouse brain section treated with MAGIC and labeled with FluoroMyelin™ red. In green and red respectively, the

71   autofluorescence and the exogenous signals are shown. Images were obtained with TPFM, scale bar = 50 μm. (g) FLIM
72   representative images during the three steps of the MAGIC protocol. Lifetime color scale is set from 550 to 1350 ps. (h)
73   Fluorescence lifetime distributions (mean ± std.err) of fiber and tissue during the MAGIC steps. (i) Box chart plot of
74   fluorescence lifetime values. (j) Raman spectra (mean ± std.err) of fiber and tissue during the MAGIC steps. (k) Glycerol
75   scores (mean ± std.err) calculated along with the three major bands (550, 850, and 1465 cm^{-1}) of the glycerol Raman
76   spectrum. Statistical significance (t-test): *$p < 0.05$, ** $p < 0.001$, *** $p < 0.0001$

77   To investigate the origin of the phenomenon, we analyzed the optical properties of mouse brain sections

78   during the three steps of the protocol. Time-resolved analysis of the emitted photons, obtained with FLIM

79   (Fluorescence-lifetime imaging microscopy)[8], highlights a fluorescence lifetime increase after glycerolization.

80   MAGIC modifies the dynamics of the fluorescence decay originating from fibers and tissue. The fluorescence

81   lifetime of the tissue decreases at values comparable to those ones obtained from PFA samples (with only

82   60±30 ps average difference), while that of the fibers remains at significantly higher values, resulting in a

83   110±40 ps difference from the corresponding PFA lifetime distribution (Figure 1g, 1h, and 1i). These findings

84   suggest that the change of the molecular environment surrounding the fluorescent molecules occurs

85   differently inside and outside the fibers. To further characterize this phenomenon, we used Raman

86   spectroscopy[9] as a tool to probe molecular content and to prove the involvement of glycerol in the

87   fluorescence emission enhancement of myelinated fibers (Figure 1j). Glycerolized tissue spectra are

88   characterized by the addition of glycerol Raman peaks around 485, 550, 850, 925, 1060, and 1465 cm^{-1}

89   (Supplementary Figure 5a), as compared to PFA samples; such spectral signatures typical of glycerol

90   disappear in the surrounding tissue after MAGIC, whereas they are preserved within myelinated fibers.

91   Conversely, no DMSO contributions (present in the first step of the protocol to enhance the penetration of

92   glycerol) were detected from the Raman spectra (Supplementary Figure 5b). A more detailed analysis based

93   on the main Raman bands of glycerol was performed to quantitatively evaluate the involvement of glycerol

94   in the process (Figure 1k). After MAGIC, myelinated fibers show, on average, a significantly smaller decrease

95   (~16%) in the intensity of glycerol-related Raman peaks with respect to the surrounding tissue (~21%). All

96   these findings indicate that the glycerol plays a central role in the MAGIC protocol. The higher fluorescence

97   lifetime measured in the fibers suggests an anti-quenching effect. Raman spectroscopy proves the

98   involvement of glycerol in the fluorescence emission of myelinated fibers. In conclusion, the fluorescence

99   enhancement could be due to the glycerol that remains confined inside the myelinated fibers after MAGIC

100   due to its higher affinity[10] to this structure with respect to the surrounding tissue.

101
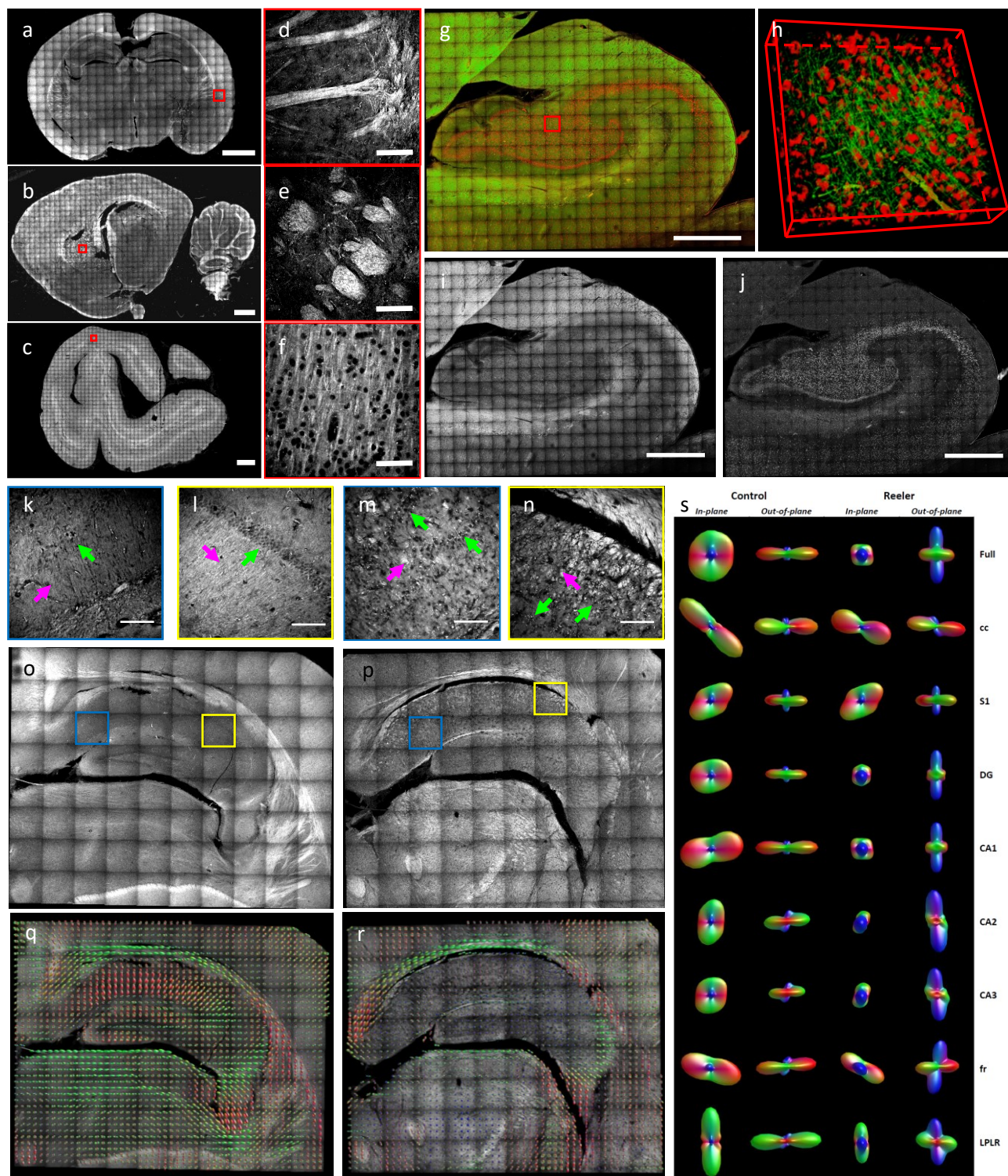
Figure 2. Mesoscopic 3D reconstruction and quantification with MAGIC. Maximum intensity projection (MIP) of the mesoscale reconstruction of 60-μm-thick brain sections treated with MAGIC: mouse (a), rat (b), and vervet monkey (c), respectively. Scale bar = 1 mm. (d, e, f) Magnified inset corresponding respectively to the red boxes in a, b, c. Scale bar = 50 μm. (g) MIP of the mesoscale reconstruction of a human hippocampus 60-μm-thick coronal section. Scale bar = 1 mm. (h) 3D rendering (450 x 450 x 60 μm^3) of the stack indicated by the red box in g. (i) Green channel showing the myelinated fibers enhanced by MAGIC. (j) The red channel of the MIP in g showing the cells' bodies autofluorescence produced by lipofuscin pigments. (k, l, m, n) Magnified inset of blue and yellow boxes in q and r, respectively. Green arrows point to neuronal cell bodies, magenta arrows to myelinated fibers. Scale bar = 50 μm. (o, p) MIP of the mesoscale reconstructions of a control and Reeler mouse hippocampus 60-μm-thick coronal section. Scale bar = 1 mm. (q, r) Images show the ODF maps obtained from analyzing the full 3D hippocampus reconstruction of the Control and the Reeler mouse, sampling 16 vectors for each ODF. (s) In-plane and out-of-plane orientation of the single ODF obtained by analyzing all the vectors of the full mosaic reconstructions and each of its ROIs. Acronyms list = Full: full field of view; cc: Corpus Callosum; S1: Primary Somatosensory Cortex; DG: Dentate Gyrus; CA1, CA2, CA3: field CA1, CA2, CA3 of hippocampus; fr: Fasciculus Retroflexus; LPLR: Lateral Posterior Thalamic Nucleus.

A significant advantage of the MAGIC protocol is its widespread applicability due to the fact that glycerol is a very common biocompatible mounting medium for tissue samples. MAGIC is highly versatile and can be successfully applied to a wide variety of samples. Brain sections from different mammal species: mouse (Figure 2a, 2d), rat (Figure 2b, 2e), vervet monkey (Figure 2c, 2f), and, more importantly, humans (Figure 2g, 2h, 2i, 2j) can be imaged after being treated with the protocol. Interestingly, the presence of lipofuscin pigments[11] in the human brain sample allowed, in combination with MAGIC, the label-free detection and the 3D reconstruction of neuronal fibers and cell bodies (Figure 2i, 2j, and Supplementary Video 4), obtaining a more comprehensive anatomical organization of the human hippocampus.

Finally, in order to demonstrate that the MAGIC protocol allows us to characterize the 3D tissue anatomy, we compared the structural organization of different regions of the hippocampus from a Control and a Reeler mouse. Reeler mouse (Reelin deficient - RELN-/- Reeler) is a well-known animal model for several neurological and neurodegenerative disorders[12,13]. In the Reeler sample, the organization of neuronal cell bodies and fibers is different compared to that of the Control mouse (Figure 2k, 2l, 2m, 2n). To quantify the observed alteration on the mesoscale reconstruction (Figure 2o, 2p), different regions of the mosaic were selected and manually segmented according to their anatomical classification (Supplementary Figure 6). A custom-made automatic Structure Tensor Analysis[14] tool followed by an Orientation Distribution Function (ODF)[15] evaluation of the derived vectors were applied to the full reconstruction and on each ROI (Figure 2q, 2r, 2s, Supplementary Figure 7). We found that the primary peaks orientation of the Control mouse is mostly constituted by in-plane contributions in all the selected ROIs, while six out of eight areas of the Reeler sample are distributed in the out-of-plane direction (Figure 2s and Table 1). These findings demonstrate that the

136 Reeler mouse's inner connectivity of the hippocampus differs significantly from the fiber organization of a

137 normal mouse.

138 **Table 1. ODF components analysis.** Amplitude (a1, a2, a3) and main orientation (direction) of the significant ODF
139 components of both Control and Reeler mouse hippocampi are shown. Table cell is gray if the peak amplitude is <50%
140 of the primary peak. Acronyms list = Full: full field of view; S1: Primary Somatosensory Cortex; cc: Corpus Callosum; CA1,
141 CA2, CA3: field CA1, CA2, CA3 of hippocampus; DG: Dentate Gyrus; fr: Fasciculus Retroflexus; LPLR: Lateral Posterior
142 Thalamic Nucleus.

ROI	CONTROL MOUSE							REELER MOUSE						
	ODF Lobes	a_1	Direction	a_2	Direction	a_3	Direction	ODF Lobes	a_1	Direction	a_2	Direction	a_3	Direction
Full	3	0.14	In-plane	0.14	In-plane	0.09	Out-of-plane	3	0.16	Out-of-plane	0.11	In-plane	0.11	In-plane
cc	1	0.35	In-plane					1	0.26	In-plane				
S1	2	0.20	In-plane	0.12	In-plane			3	0.17	In-plane	0.11	In-plane	0.11	Out-of-plane
DG	1	0.16	In-plane					1	0.19	Out-of-plane				
CA1	1	0.23	In-plane					2	0.18	Out-of-plane	0.09	In-plane		
CA2	1	0.18	In-plane					1	0.24	Out-of-plane				
CA3	2	0.15	In-plane	0.08	Out-of-plane			1	0.20	Out-of-plane				
fr	1	0.23	In-plane					2	0.21	Out-of-plane	0.18	In-plane		
LPLR	1	0.30	In-plane					2	0.18	Out-of-plane	0.16	In-plane		

143 To conclude, the methodology presented here demonstrated the possibility of reconstructing the

144 organization of myelinated fibers over large volumes in 3D at sub-micron resolution, enabling the study of

145 the brain anatomy in both physiological and pathological conditions, thus offering a reliable method for

146 integrated quantitative analyses. The versatility and simplicity of MAGIC will enable easy implementation of

147 the technique in many laboratories, offering the possibility of using 3D investigation for routine analysis. We

148 believe that MAGIC will help to have a more profound comprehension of the brain structure, bringing a

149 significant impact on neuroscience.

Methods

150

Specimen collection

151

152 The investigated brain sections were obtained from postmortem brains from different species: mouse

153 (control C57BL/6 and Reelin-deficient mouse model - RELN-/- Reeler, male, six months old), rat (Wistar, male,

154 three months old), vervet monkey (African green monkey: Chlorocebus aethiops sabaeus, male, between

155 one and two years old), and human (male, 87 years). The procedures for rodents were approved by the

156   institutional animal welfare committee at Forschungszentrum Jülich GmbH, Germany, and were in

157   accordance with the European Union guidelines for the use and care of laboratory animals. All methods were

158   carried out in accordance with relevant guidelines and regulations. The vervet monkey tissue sample was

159   acquired in the project "Postnatal development of cortical receptors and white matter tracts"

160   (4R01MH092311-05) funded by the NIMH of the National Institutes of Health. The project was carried out in

161   accordance with the UCLA Chancellor's Animal Research Committee ARC #2011-135 and by the Wake Forest

162   Institutional Animal Care and Use Committee IACUC #A11-219. The human brain was acquired in accordance

163   with the ethics committee at the Medical Faculty of the University of Rostock, Germany #A2016-0083.

MAGIC preparation protocol

165   Brains from different species (mouse, rat, vervet, and human) were fixed with 4% paraformaldehyde (PFA)

166   solution at 4°C for several weeks (human brain: >3 months, vervet, rat, and mouse brains: 1–2 weeks). The

167   brains were embedded first in a 10% glycerol, 2% DMSO, 4% formaldehyde solution at +4°C, then in a 20%

168   glycerol, 2% DMSO, 4% formaldehyde solution at +4°C for mouse and rat brains 7 days in total, while for

169   vervet and human brains ≥ 3 weeks. After treatment with 2% dimethyl sulfoxide for cryoprotection, brains

170   were dipped in cooled isopentane (-50°C) for several minutes (mouse and rat brains: >5min, human and

171   vervet brains: >30min). The frozen brains were cut with a cryostat microtome (Leica Microsystems, Germany)

172   at a temperature of -30°C into sections of approximately 60 μm thickness. Brains were cut along one of three

173   mutually orthogonal, anatomical planes: coronal, horizontal, or sagittal. Finally, the brain sections were

174   incubated in a Phosphate Buffer Saline solution (PBS) 0.01M at room temperature (RT) for one month for

175   mouse and rat brains and three months for vervet and human brains. Before imaging, the sections were

176   mounted with PBS and coverslipped. For myelin characterization, the labeling was performed using the

177   FluoroMyelin^{TM} red dye (Thermo Fisher Scientific, cat. num. F34652): mouse brain sections were incubated

178   in a solution of 1:300 FluoroMyelin^{TM} in PBS for 20 minutes at room temperature. Then sections were rinsed

179   3 times for 10 minutes each with PBS.

Fluorescence microscopy imaging

181 Fluorescence images were obtained using a commercial confocal microscope (Nikon Eclipse TE300 C2 LSCM,

182 Nikon, Japan) equipped with a Nikon 60× or 100× immersion oil objective (Apo Plan, NA 1.4), and a custom-

183 made two-photon fluorescence microscope (TPFM) at room temperature. Briefly, a mode-locked Ti: Sapphire

184 laser (Chameleon, 120 fs pulse width, 90 MHz repetition rate, Coherent, CA) operating at 800 nm was coupled

185 into a custom-made scanning system based on a pair of galvanometric mirrors (LSKGG4/M, Thorlabs, USA).

186 The laser was focused onto the specimen by a refractive index tunable 25x objective lens (LD LCI Plan-

187 Apochromat 25X/0.8 Imm Corr DIC M27, Zeiss, Germany) set either to glycerol or water. The imaged field of

188 view was of 450×450 µm^2, the resolution employed was 0.44×0.44 µm^2 or 1.75×1.75 µm^2. The system was

189 equipped with a closed-loop XY stage (U-780 PILine® XY Stage System, Physik Instrumente, Germany) for the

190 radial displacement of the sample and with a closed-loop piezoelectric stage (ND72Z2LAQ PIFOC objective

191 scanning system, 2 mm travel range, Physik Instrumente, Germany) for the displacement of the objective

192 along the z-axis. The fluorescence signal was collected by an independent GaAsP photomultiplier module

193 (H7422, Hamamatsu Photonics, NJ). Emission filters of 482/35 nm and 618/50 nm were used for fibers and

194 cell body detection, respectively.

Mesoscale reconstruction

196 To perform mesoscale reconstruction of the samples, the volume of interest was acquired with TPFM

197 performing z-stack imaging of adjacent regions using a custom LabView program (National Instruments). The

198 8-bit images (1024 x 1024 px or 256 x 256 px) produced were saved in .tiff format. Each stack was acquired

199 with a depth equal to the thickness of the section (50 ± 10 µm) and with a z step of 1 or 2 µm between images.

200 Each frame had a field of view of 450×450 µm^2 and a pixel size of 0.44×0.44 µm^2 or 1.75×1.75 µm^2 for low-

201 resolution reconstruction. The overlap of adjacent stacks was set as 40 µm. The stitching of all the acquired

202 stacks was performed using ZetaStitcher (G. Mazzamuto, "ZetaStitcher: a software tool for high-resolution

203 volumetric stitching" https://github.com/lens-biophotonics/ZetaStitcher). Low-resolution reconstructions

204 were performed on the mouse coronal section, the rat sagittal section, and on the vervet section. High-

205   resolution imaging was performed on the human hippocampus section and on the Reeler and control coronal

206   section.

Photon counting and Fluorescence Lifetime Imaging Microscopy (FLIM) measurements

208   FLIM measurements were performed on different mouse brain sections (N=15) during the three conditions

209   of the protocol (samples: PFA N=4, Gly N=6, and MAGIC N=5) using a custom-made multimodal setup[16]. The

210   collected fluorescence was sent to a high-speed PMT for photon counting PMH-100 (Becker-Hickl GmbH,

211   Berlin, Germany) and then processed by a single-photon counting FLIM board SPC-730 (Becker-Hickl GmbH)

212   for time-resolved analysis. Analysis of the obtained FLIM images was performed using the software SPC

213   Image 4.9.7 (Becker-Hickl GmbH, Berlin, Germany), fitting the fluorescence decay data with a double-

214   exponential decay function. From each image, we selected ROIs (10 for PFA, 12 for Gly, 8 for MAGIC)

215   corresponding to the myelin sheath and the surrounding brain tissue in order to analyze the distribution of

216   their lifetime values separately. The photon-counting obtained from the same samples were also used to

217   evaluate the fluorescence efficiency of the MAGIC protocol. We measured the fluorescence intensity at

218   different excitation wavelengths (from 740 nm to 880 nm), and we normalized it to the square of the

219   respective laser power. For each condition, we selected the maximum amount of 240 μm^2 ROIs detectable

220   from the sample: 43 and 56 for PFA tissue and fibers respectively, 49 and 38 for Gly, 68 and 62 for MAGIC.

221   Contrast evaluation was performed by dividing the fluorescence intensity detected from myelin fibers by that

222   of the surrounding tissue.

Fluorescence spectral measurements

224   The multimodal microscope, set at an excitation wavelength of 800 nm, was used to perform the spectral

225   analysis measurements. Autofluorescence signals were collected during the three conditions of the protocol

226   (N=1 sample for each step). The collected fluorescence signal was coupled to a multimode optical fiber by

227   means of a 10× objective lens (Nikon, Tokyo, Japan) and detected in the 420-620 nm range using a

228   multispectral detector PML-Spec (Becker-Hickl GmbH, Berlin, Germany) with 16 spectral channels. Each

229   channel recorded a fluorescence intensity image in 90 s, from which we selected regions of interest (ROIs)

230   corresponding to the myelin sheath (N=3) and the surrounding brain tissue (N=3) in order to analyze the

231   intensity of their fluorescence emission separately.

Raman measurements

233   We used a commercial Raman microscope (XploRA INV, Horiba, Kyoto, Japan) with λ_{EX} = 532 nm for collecting

234   the Raman spectra of mouse brain tissues during the three conditions of the protocol on both the myelin

235   sheath and the surrounding tissue (N=4 samples for each step). For each acquisition, we used a 60× objective

236   (Nikon, Tokyo, Japan) for scanning a 10-µm-area while recording the Raman signal between 400 and 1750

237   cm^{-1} with 1800 lines/mm grating: each measurement lasted 30 s. The recorded spectra were processed to

238   remove the fluorescence signal through an automated iterative routine (Vancouver Raman Algorithm). Each

239   resulting Raman spectrum was normalized to its maximum intensity. Then, in order to evaluate the glycerol

240   content within the examined tissue areas, we performed a spectral projection of all Raman spectra along

241   with three major bands (550, 850 and 1465 cm^{-1}) of glycerol; in particular, we calculated the scalar product

242   between the spectra and the Raman peaks recorded from the glycerolized mounting medium solution. From

243   that, for each spectrum, we obtained a score ("glycerol score") equal to 1 for glycerolized tissues and <1

244   otherwise.

Data analysis

246   Graphs   and   statistical   analyses   were   done   with   OriginPro   9.0   (OriginLab   Corporation)   and

247   www.socscistatistics.com. Mean and standard errors are displayed for each chart. Statistical analyses were

248   performed using a one-tailed two-sample t-test. For the mean lifetime measurement the p-value (p), Cohen's

249   d (d), degrees of freedom (DF), and mean difference (m) ± confidence interval (CI) at 95% are: PFA fiber vs

250   PFA tissue: p = 0.00028, d = 1.872, DF = 18 , m+-95% CI = 98 ± 49; Gly fiber vs Gly tissue: p = 0.00041, d =

251   1.653, DF = 20, m+-95% CI = 109 ± 58; Magic fiber vs Magic tissue: p = 0.00009, d = 2.493, DF = 14, m+-95%

252   CI = 150 ± 64. For the Magic fiber vs Magic tissue glycerol-score evaluation: p = 0.0173, d = 1.923, DF = 6, m+-

253   95% CI = 0.06 ± 0.05. Stacks and 3D stitched volume renderings and videos were obtained using both Fiji

254   (http://fiji.sc/Fiji) and Amira 5.3 (Visage Imaging).

Structure tensor analysis (STA) evaluation

255

256 Following the preprocessing operations detailed in the Supplementary information, a structure tensor

257 analysis (STA) was conducted at 5 µm spatial resolution on the whole mesoscale reconstruction of the

258 hippocampus and separately on the selected ROIs (Figure 2 and Supplementary Fig.6) for estimating the local

259 brain tissue orientation. To this end, we employed a custom STA tool developed by our laboratory in the

260 framework of the European Human Brain Project. The source code of the present tool, written in Python3,

261 can be accessed at: https://github.com/lens-biophotonics/st_fibre_analysis_hbp.

262 In order to reject background and spurious dark regions, retaining only the contribution of brain structures,

263 and improve the reliability of the obtained vector fields, a threshold of 85% non-zero voxels was imposed

264 beforehand on each 5-µm macro-voxel to be characterized.

265 In detail, local gradient-square tensors were first computed as the outer product of the image gradient ∇I

266 with itself:

$$S_v(x, y, z) = \nabla I \nabla I^T = \begin{pmatrix} I_x^2 & I_x I_y & I_x I_z \\ I_x I_y & I_y^2 & I_y I_z \\ I_x I_z & I_y I_z & I_z^2 \end{pmatrix},$$

267

268 where I_x , I_y and I_z respectively denote the local first-order spatial derivatives along the x, y, and z axes.

269 Tensor elements estimated voxel-wise were then averaged over 5-µm local neighborhoods after isotropic

270 smoothing by means of Gaussian kernels g_{σ_s} with standard deviation $\sigma_s = 3$ pixel.

271 3D tissue orientation maps were finally derived from the local directions of minimal gray level change, i.e.

272 the eigenvector of the averaged structure tensor $\bar{S}_{\sigma_s}$ associated with the lowest eigenvalue.

Orientation Distribution Functions (ODF) calculation

273

274 Fiber orientation distribution functions (ODFs) were used to characterize a given distribution of 3D

275 orientations, i.e., nerve fibers. To calculate the ODF of a given number of K orientation vectors, the individual

276 spherical harmonic (SH) coefficients c_{lm} of the ODF were estimated as $c_{lm} = \frac{N_l^m}{K} \sum_{k=1}^{K} P_l^m \cos(\theta_k) e^{-im\varphi_k}$

277 with N_l^m as the normalization coefficient, P_l^m as Legendre polynomes, φ as azimuthal, and θ as the polar

278 angle. This calculation was applied to the orientations obtained in a super-voxel consisting of $n_x \times n_y \times n_z$

279   voxels. In particular, to represent the ODFs of figure 2q and 2r a super voxel of 16 x 16 x 8 vectors,

280   corresponding to a cube of 80 x 80 x 40 μm, was selected; while to obtain the total ODF of the full

281   reconstruction and of the selected ROIs (represented in figure 2s), all the vectors present in the section were

282   considered. The visualization of the ODFs was done with the open-source tool mrview from MRtrix3[17]. To

283   avoid boundary artefacts, only super-voxels containing at least 1/3 of the total evaluated orientations were

284   shown. The size of the ODFs was scaled by a factor of 2 to improve their visibility. Next, the MRtrix3 sh2peaks

285   tool was applied to the obtained SH images in order to extract the Cartesian components of the three

286   principal ODF lobes and, then, determine their amplitude (Euclidean norm). At this stage, amplitude values

287   below 50% of the largest peak of the ODF were discarded, with the aim to exclude minor maxima related to

288   noise from further consideration.

Acknowledgments

Author contributions

I.C. developed MAGIC, designed all the experiments, performed sample preparation, and conducted TPFM imaging. I.C and E.B performed the validation experiments. E.B and R.C analyzed the validation data. G.M developed the ZetaStitcher software and performed the mesoscopic reconstruction. F.G wrote the STA software. M.S evaluated the mesoscopic reconstruction with the STA software. F.M, M.M, and M.A effectuated the ODFs analysis. K.A and M.A provided the tissue specimens and contributed to the concept of the study. I.C, L.S, M.A, K.A, and F.S.P. supervised the project. I.C. made the figures and wrote the paper with inputs from all authors.

Competing financial interests

The authors declare that they have no competing financial interests.

Data availability

All data supporting the findings of this study are included in figures and videos as representative images or data points in the plots. Additional images other than the representative images are available from the corresponding author upon reasonable request.

Code availability

MRtrix3 is an open source tool; ZetaStitcher and STA codes are open source and available on GitHub at URLs provided in the Methods. The other custom code used in this study are available from the corresponding author upon reasonable request.

References

1   Aggarwal, S., Yurlova, L. & Simons, M. Central nervous system myelin: structure, synthesis and assembly. *Trends Cell Biol* **21**, 585-593, doi:10.1016/j.tcb.2011.06.004 (2011).

2   Giacci, M. K. *et al.* Three dimensional electron microscopy reveals changing axonal and myelin morphology along normal and partially injured optic nerves. *Scientific reports* **8**, 3979, doi:10.1038/s41598-018-22361-2 (2018).

3   Heath, F., Hurley, S. A., Johansen-Berg, H. & Sampaio-Baptista, C. Advances in noninvasive myelin imaging. *Dev Neurobiol* **78**, 136-151, doi:10.1002/dneu.22552 (2018).

4   Hajjar, H. *et al.* Label-free non-linear microscopy to measure myelin outcome in a rodent model of Charcot-Marie-Tooth diseases. *J Biophotonics* **11**, e201800186, doi:10.1002/jbio.201800186 (2018).

5   Lai, H. M., Ng, W. L., Gentleman, S. M. & Wu, W. Chemical Probes for Visualizing Intact Animal and Human Brain Tissue. *Cell Chem Biol* **24**, 659-672, doi:10.1016/j.chembiol.2017.05.015 (2017).

6   Costantini, I., Cicchi, R., Silvestri, L., Vanzi, F. & Pavone, F. S. In-vivo and ex-vivo optical clearing methods for biological tissues: review. *Biomed Opt Express* **10**, 5251-5267, doi:10.1364/BOE.10.005251 (2019).

7   Monsma, P. C. & Brown, A. FluoroMyelin Red is a bright, photostable and non-toxic fluorescent stain for live imaging of myelin. *J Neurosci Methods* **209**, 344-350, doi:10.1016/j.jneumeth.2012.06.015 (2012).

8   Becker, W. Fluorescence lifetime imaging--techniques and applications. *J Microsc* **247**, 119-136, doi:10.1111/j.1365-2818.2012.03618.x (2012).

9   Morisaki, S. *et al.* Application of Raman spectroscopy for visualizing biochemical changes during peripheral nerve injury in vitro and in vivo. *J Biomed Opt* **18**, 116011, doi:10.1117/1.JBO.18.11.116011 (2013).

10   Ledeen, R. W. & Haley, J. E. Axon-myelin transfer of glycerol-labeled lipids and inorganic phosphate during axonal transport. *Brain Res* **269**, 267-275, doi:10.1016/0006-8993(83)90136-1 (1983).

11   Terman, A. & Brunk, U. T. Lipofuscin. *Int J Biochem Cell Biol* **36**, 1400-1404, doi:10.1016/j.biocel.2003.08.009 (2004).

12   Deller, T. *et al.* The hippocampus of the reeler mutant mouse: fiber segregation in area CA1 depends on the position of the postsynaptic target cells. *Exp Neurol* **156**, 254-267, doi:10.1006/exnr.1999.7021 (1999).

13   Lossi, L., Castagna, C., Granato, A. & Merighi, A. The Reeler Mouse: A Translational Model of Human Neurological Conditions, or Simply a Good Tool for Better Understanding Neurodevelopment? *J Clin Med* **8**, doi:10.3390/jcm8122088 (2019).

352 14   Kowalski, W. J. *et al.* Quantification of Cardiomyocyte Alignment from Three-Dimensional (3D)
353   Confocal Microscopy of Engineered Tissue. *Microsc Microanal* **23**, 826-842,
354   doi:10.1017/S1431927617000666 (2017).
355 15   Axer, M. *et al.* Estimating Fiber Orientation Distribution Functions in 3D-Polarized Light Imaging.
356   *Front Neuroanat* **10**, 40, doi:10.3389/fnana.2016.00040 (2016).
357 16   Marchetti, M., Baria, E., Cicchi, R. & Pavone, F. S. Custom Multiphoton/Raman Microscopy Setup
358   for Imaging and Characterization of Biological Samples. *Methods Protoc* **2**,
359   doi:10.3390/mps2020051 (2019).
360 17   Tournier, J. D. *et al.* MRtrix3: A fast, flexible and open software framework for medical image
361   processing and visualisation. *Neuroimage* **202**, 116137, doi:10.1016/j.neuroimage.2019.116137
362   (2019).

363